Materials Advances

ROYAL SOCIETY OF CHEMISTRY

PAPER

View Article Online
View Journal

Cite this: DOI: 10.1039/d5ma01448d

A polymer wire wetware synapse with improved endurance for physical neuromorphic implementation

Adrian D. Go, Seiya Watanabe, Hiroyuki S. Kato and Megumi Akai-Kasaya*

Neuromorphic computing requires synaptic devices that can reliably update and retain weights under repeated electrical stimulation. Among the material platforms being explored for this purpose, organic wetware synaptic systems are of interest because their switching behavior is directly influenced by the surrounding electrochemical environment. Herein, we report a two-terminal (hydroxymethyl)-3,4-ethylenedioxythiophene:sodium dodecyl benzene sulfonate (PEDOT–MeOH:SDBS) polymer-wire synaptic device operated in ethylene glycol (EG) and water. The device exhibits long-term synaptic plasticity induced by repeated voltage pulses. Under EG operation, the device endures ≥1000 bidirectional conductance switching cycles with stable cyclic voltammetry features and reduced charge-transfer resistance after cycling. In contrast, aqueous operation leads to switching endurance degradation, peak shifts in *I*–*V* curve, and increased charge-transfer resistance. Scanning electron microscopy and Raman spectroscopy showed that EG operation is associated with a granular surface morphology and comparatively preserved backbone structure, whereas aqueous operation leads to smoother, more deteriorated surface features, and increased structural disorder. To demonstrate device applicability, conductance states of the polymer wires were mapped to kernels in a convolutional neural network (CNN) for digit recognition, achieving 96% accuracy after 450 epochs. The findings show that operation in EG improves the switching endurance of PEDOT–MeOH:SDBS polymer-wire synapse and that their conductance states can be implemented as physical weights for neural networks. This work highlights electrochemical media engineering as a key design strategy for scalable neuromorphic platforms.

Received 11th December 2025,
Accepted 6th May 2026

DOI: 10.1039/d5ma01448d

rsc.li/materials-advances

1. Introduction

Artificial intelligence (AI) has permeated various sectors of society for automated tasks such as image recognition, language processing, robotics, and data analytics.[1,2] This rapid expansion has intensified the demand for hardware capable of supporting more efficient computation.[3] The limitations caused by Von Neumann-based technology have become increasingly apparent in recent years. The Von Neumann architecture is well recognized to have challenges in terms of high energy costs and scalability due to the physical separation of memory and processing units during data transfers.[4] In response to this issue, neuromorphic computing provides an alternative brain inspired paradigm that mimics biological network processes. This architecture offers the integration of memory and computation within the same system, which avoids the process of data shuffling back and forth.[5,6] This allows reduced energy consumption and true parallel processing for the next generation of artificial intelligence.

Neuromorphic systems are generally implemented through synaptic devices that serve as artificial analogs of the biological synapses.[7] These devices can emulate biological synapses (memory storage, recognition, and learning) *via* storing and updating weights *in situ* in response to defined learning rules. Conventional solid-state synaptic devices, including oxide memristors,[8] phase-change materials,[9] and ferroelectric transistors,[10] have already demonstrated substantial progress in reproducing synaptic plasticity and in enabling bio-integrated electronic systems.[11] In parallel with these developments, organic electrochemical devices have attracted increasing interest as neuromorphic platforms because they provide access to a distinct operating regime in which switching behavior is governed by coupled ionic and electronic processes.[12] In such systems, device behavior can be tuned not only through material composition and geometry but also through the electrochemical medium itself, which provides an additional route for engineering analog weight modulation and device response.[13]

Department of Chemistry, Graduate School of Science, The University of Osaka, Osaka, Japan. E-mail: akai@chem.sci.osaka-u.ac.jp

Within this broader class, wetware systems are especially useful because the active element is directly exposed to the surrounding liquid environment during operation. As a result, the operating medium becomes a key design variable that can strongly influence the switching characteristics, endurance, retention, and degradation. This creates opportunities and challenges that are not captured by conventional dry solid-state architectures.

Poly(3,4-ethylenedioxythiophene) doped with poly(styrene sulfonate) (PEDOT:PSS) is a popular conductive polymer for organic electronics because of its low-cost, tuneable properties, and high conductivity.[14] However, the PSS bears acidic sulfonic groups, which drive interfacial corrosions and swelling under liquid operation.[15,16] This drawback motivates molecular functionalization like dopant engineering or EDOT ring substitution to mitigate acidity and swelling while preserving conductivity.[17] Specifically, 3,4-ethylenedioxythiophene methanol (EDOT–MeOH) is a derivative of EDOT containing a hydroxymethyl substituent on the 3,4-position of the thiophene ring that has improved solubility in aqueous media.[18] The hydroxymethyl groups form intermolecular hydrogen bonding between the monomer units and polar dopants, which creates an interconnected structure that enhances doping efficiency and stability.[19] Moreover, studies showed enhanced biocompatibility when using such materials for modified electrochemical sensors.[20,21] To date, there are limited investigations on PEDOT–MeOH as an active material for synaptic devices, particularly in wet-operating environments that demand endurance under continuous electrochemical stimulation.

Recent PEDOT-based neuromorphic systems have already demonstrated diverse plasticity functions in electrolyte synapses,[22] organic electrochemical transistors (OECTs),[23] and organic memristive devices.[24] These types of devices have shown long-term plasticity and long state retention.[25–27] In addition, two-terminal PEDOT:PSS wire devices[28] and electropolymerized PEDOT:PSS fiber networks[29] have expanded the range of wet-operating and structural-plasticity neuromorphic platforms. Polymer-wire architectures have also been shown to support 3D spatially distributed conductive structures, as demonstrated in our previous study.[30] Such systems are attractive since they can support more spatially distributed connectivity and higher wiring density, which are desirable features for brain-inspired device architectures. Building on this broader PEDOT-based neuromorphic landscape, the present study examines a suspended two-terminal PEDOT–MeOH:SDBS polymer-wire architecture directly operated in ethylene glycol (EG) as the active organic liquid medium. In contrast to the predominantly planar and gate-controlled operation of many PEDOT-based OECT and memristive systems, this configuration enables explicit investigation of how the liquid operating medium influences repeated conductance switching, endurance, and stability while preserving the possibility for non-planar wiring configurations.

Herein, we report a two-terminal PEDOT–MeOH:SDBS polymer-wire synaptic device suspended in ethylene glycol (EG) that exhibits repeated conductance switching (potentiation and depression) over 1000 cycles. Although EG is commonly used as a post-treatment additive to enhance the electrical conductivity of conducting polymers,[31,32] the present system functions as the operating electrochemical medium during device operation. We investigated the electrochemical switching behavior of the device together with the associated structural and electrochemical changes in the polymer. To examine functional applicability, the conductance states of the polymer wire were mapped as analog kernel weights in a proof-of-concept convolutional neural network (CNN) architecture.

2. Experimental

2.1 Materials and reagents

The reagents used in this study were 2-(hydroxymethyl)-3,4-ethylenedioxythiophene (EDOT–MeOH, >98%, Sigma-Aldrich, USA), sodium dodecyl-benzene sulfonate (SDBS, Pharmaceutical Secondary Standard, Sigma-Aldrich, USA), ethylene glycol (EG, ≥99.5%, Sigma-Aldrich, USA), tetrabutyl ammonium perchlorate (TBAP, ≥98.0%, Tokyo Chemical Industry, Japan), and sodium nitrate (≥99.0%, Sigma-Aldrich, USA). The chemicals were used without additional purification.

2.2 Fabrication of the polymer-wire-based synaptic device

An electrode pair was fabricated on a 2.5 × 2.5 mm^2 micro slide glass substrate (Matsunami Glass Industry, Japan). Photoresists exposed to an LED lithography MLA 150 (Heidelberg Instruments, Germany) maskless aligner were used to pattern the glass. Then, the substrate was sputtered using a Canon Anelva EB1100 (Canon Anelva Corporation, Japan) with multilayer metal coats consisting of a 10 nm Ti intermediate layer, and a 400 nm Au contact layer. The fabricated electrode featured a 150 μm gap between the two sharp tips. Device operation and conductance measurements were performed on a microprobe station equipped with an Olympus SZX7 optical microscope (Olympus Corporation, Japan) as illustrated in Fig. 1a. Operation of voltage control and voltage pulse application was achieved through a two-terminal system with the metal probes contacted to the working and counter electrodes. A mechanical relay board controlled by an Arduino Mega 2560 (Arduino LLC, Italy) was used to regulate the timing of V_{input} (for conductance modulation) and V_{read} (for conductance measurement). A detailed explanation was provided in our previous study.[28,33]

A precursor solution of 0.135M EDOT–MeOH and 0.02M SDBS dissolved in ultrapure water was prepared. Then, 5 μL of the precursor solution was dispensed between the two electrode tips. Polymer wire growth was performed by applying alternating bipolar square AC voltage (12 V_{p-p}, 5 kHz, 50 duty cycle) using a WF1973 wavefunction generator (NF Corporation, Japan) connected to an HSA 4011 high speed bipolar amplifier (NF Corporation, Japan). The polymer wire was allowed to grow horizontally until full connection (see SI Video S1). Next, the polymer wire was made thicker on one side with 200 pulses of +2.5 V DC (20 ms width) to induce its synaptic properties (see SI Video S2). Asymmetric formation of the polymer wire was observed after 200 pulses of +2.5 V DC. Then, the residual

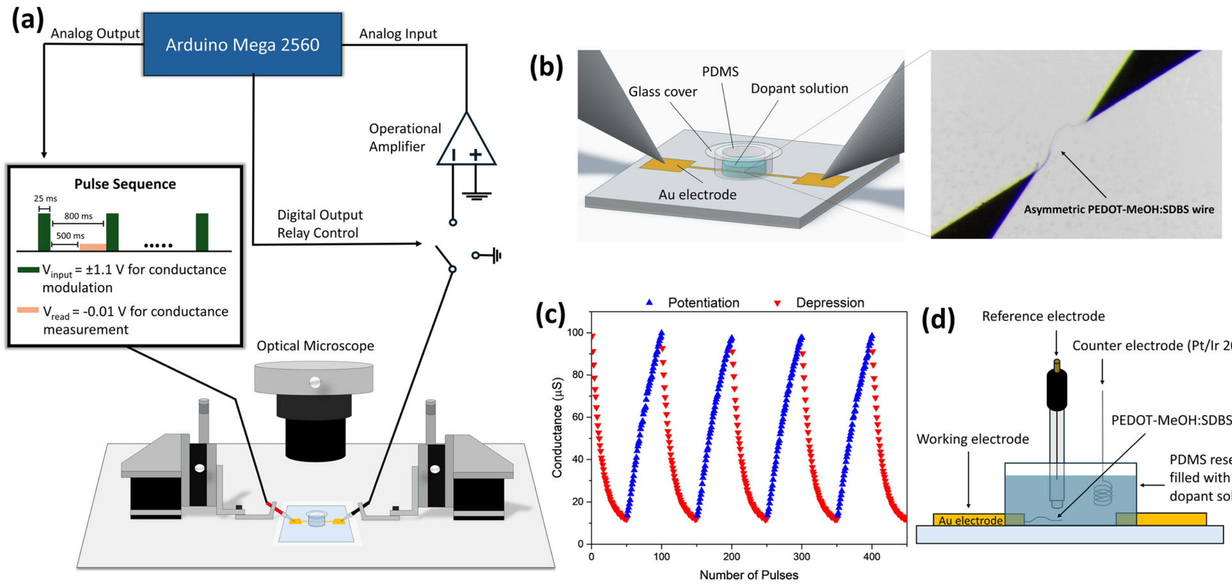

Fig. 1 Schematic of the experimental setup. (a) Probe station for the conductance modulation and measurement of the polymer wire device, (b) polymer wire device with a magnified view of the polymer wire grown between electrodes, (c) conductance modulation polymer wire device using ±1.1 V pulse application resulting in potentiation and depression cycles, (d) setup of the three-terminal electrode system for the electrochemical characterization of the polymer wire.

solution was removed, and the wire was rinsed with distilled water and dried. A polydimethylsiloxane (PDMS) reservoir was affixed to the glass substrate where the polymer wire was centered inside. The PDMS reservoir was filled with 20 µL of 0.02 M SBDS in EG or water as shown in Fig. 1b and c. Modulation of the conductance (V_{input}) was carried out by 50 pulses of +1.1 V DC (25 ms pulse width) for potentiation and 50 pulses of −1.1 V DC (25 ms pulse width) for depression (Fig. 1c) at intervals of 500 ms. The counter electrode was grounded during the application of these pulses. Between pulses, the counter electrode was switched to the measurement circuit wherein a small voltage of −0.01 V (V_{read}) was applied through an operational amplifier (gain = 2.0 × 10^6 V A^{-1}). Current was computed from the output voltage of the TIA circuit and conductance was calculate from $G = I/V_{\mathrm{read}}$. All reported conductance values represent the average of 50 consecutive measurements.

2.3 Physical and electrochemical characterization

Vibrational signatures of the polymer wire were evaluated with an NRS-3100 Raman microscope (JASCO, Japan) for structural changes at 750 to 1800 cm^{-1} (532 nm laser). The surface morphology of the polymer wire was observed using a JSM-7600F SEM (JEOL Ltd, Japan). The polymer wire samples were cleaned with acetonitrile wash and dried prior to the analysis.

A three-electrode system was constructed for electrochemical characterization (Fig. 1d). Conductive polymer wires were grown according to Method 2.2 with adjustments to the AC bias (0.7 $V_{\mathrm{p-p}}$, 5 kHz, +0.2 V offset, 50% duty), allowing polymer growth only from one side of the electrode. Then, the solution was removed and was replaced with 200 µL of 0.02 M SBDS in EG (0.01 M TBAP supporting electrolyte) or 0.02 M SDBS in water (0.01 M $NaNO_3$ supporting electrolyte) contained in a PDMS reservoir. For EG media, an Ag/Ag^+ reference electrode (BAS, Japan) filled with EG containing 0.01 M $AgNO_3$ and 0.1 M TBAP was used. Whereas reference electrode Ag/AgCl with 3 M NaCl internal solution (BAS, Japan) was employed for aqueous systems. A coiled Pt/Ir (20%) wire served as the counter electrode for both media. Cyclic voltammetry and electrochemical impedance spectroscopy (EIS) measurements were performed with an ALS/HCH 7082E electrochemical analyzer (BAS, Japan).

2.4 CNN Machine learning implementation

A CNN was implemented to evaluate polymer-wire synapses in a hardware-in-the-loop setting (Fig. S5). Training inputs were 5 × 5 binary digit images (−1, +1) spanning 10 classes (0–9) (Fig. S6). Sixteen polymer wires were fabricated and each conductance state of the polymer wire served as a direct weight for the CNN kernels (3 × 3) (Fig. S7). Individual polymer wire-based synaptic device channels were independently controlled through a photorelay switch managed by an Arduino Mega 2560 microcontroller. Kernel weight programming used a program-and-verify loop with ±1.1 V write pulses and per-pulse adjustments. Each weight update was terminated at ±1% error from target conductance or after 100 iterations. Conductance was measured by applying −0.01 V and reading the current output through a TIA circuit (gain = 4.7 × 10^6). On each step, the 5 × 5 input was convolved with the 3 × 3 kernels (stride = 1). Feature maps were reduced by global average pooling to five scalar features and were fed to a fully connected layer (5 × 10) with 10 biases to produce logits. Softmax activation was used to convert logits to class probabilities. Cross-entropy loss was computed against one-hot labels. The fully connected parameters were updated by stochastic gradient descent (learning rate = 0.02). Then, the target kernel values were mapped to the conductance state of the polymer wires. The updated kernel weights were used for the next training cycle until 450 epochs were reached. Accuracy and loss function were recorded to evaluate the learning model.

3. Results and discussion

3.1 Conductance switching and endurance of the polymer wire device

Artificial synaptic devices aim to produce adaptive weight updates of biological synapses. Biological plasticity can be categorized into short-term plasticity (STP) and long-term potentiation and depression (LTP/D). STP refers to the transient changes in synaptic strength that briefly occur in milliseconds based on the presynaptic mechanism, such as calcium accumulation and vesicle depletion.[34] This plays a role in rapid signal processing and temporal coding. However, the volatile nature of STP limits its use for retaining information. LTP/D, on the other hand, corresponds to the persistent strengthening of synaptic connections lasting from hours to lifetime driven by post-synaptic regulation and organization. LTP/D is the biological basis for long term learning memory formation. In the context of neuromorphic devices, LTP/D is recognized to be more critical than STP since it enables cumulative weight updates needed for learning tasks such as image and digit recognition. The practical realization of LTP/D hinges on device endurance, which is defined as the ability to undergo repeated conductance updates without failure. High switching endurance is therefore a core requirement.

In this work, the polymerization of the PEDOT–MeOH:SDBS wire was achieved in between the electrode by application of AC bias. Subsequent DC pulses above its oxidation potential formed an asymmetric area on one side of the wire. The observed LTP/D upon DC bias pulses is explained by the electrochemical doping and dedoping process of the polymer involving the ion transport in the electrolyte. When pulses of positive bias are applied, PEDOT^0–MeOH is oxidized to PEDOT$^+$ and the SBDS counterions acts as a dopant stabilizer to the positive charges in the polymer backbone. The reverse happens when applying negative voltage bias, wherein the PEDOT$^+$–MeOH is reduced back to PEDOT^0–MeOH and is accompanied by the migration of cations to the wire to maintain electrical neutrality.[28] The overall redox equation is described in eqn (1).

$$\text{MeOH–PEDOT}^{+}\text{:SDBS}^{-} + e^{-} \rightleftharpoons \text{MeOH–PEDOT}^{0} + \text{SDBS}^{-} \quad (1)$$

Since the application of DC bias pulses resulted in the thickening of one side of the polymer wire, the conductance updates upon DC bias modulation (potentiation–depression) arise from the asymmetric and inefficient doping and dedoping process across the thicker and thinner regions. This asymmetry alters the total number of mobile charge carriers along the wire and thereby changes its overall conductance after voltage application.[33] We initially investigated the switching endurance of the polymer wire by applying several bidirectional cycles. Each cycle consisted of one potentiation phase (50 pulses of +1.1 V) followed by a depression phase (50 pulses of −1.1 V), operated in water or EG (Fig. 2a and b). For the water media (Fig. 2b), it starts with a large switching window (∼160 μS) followed by a marked decrease in the maximum conductance, which was observed immediately starting on the second cycle. The conductance of the polymer wire operated in water rapidly degraded over successive cycles, eventually leading to the collapse of the maximum conductance to <11 μS. However, operation in EG (Fig. 2a) produced a lower initial switching window (∼70–80 μS) but exhibited a more stable conductance evolution across repeated switching cycles. EG retained distinct conductance states over 1000 switching cycles, indicating enhanced endurance and electrochemical stability. To examine whether the improved endurance in EG arose simply from differences in operating voltage, the water-operated device was also tested at a reduced voltage of ±0.8 V (Fig. S1) to yield a comparable maximum conductance to EG. Under this condition, degradation was slower and the switching range was also reduced, which indicates that the improved endurance in EG cannot be explained solely by the applied voltage. The results show a trade-off between initial switching window range and long-term operational stability. Operation in water enables larger initial conductance changes while EG appears to mitigate progressive degradation during repeated electrical stimulation. EG is widely incorporated as a secondary additive or post-treatment to enhance the electrical conductivity of the conducting polymers. In contrast, the EG in this system acts as the operational liquid medium during voltage bias. This distinction is critical since EG directly participates in the electrochemical media rather than simply modifying the polymer microstructure/properties during post processing.

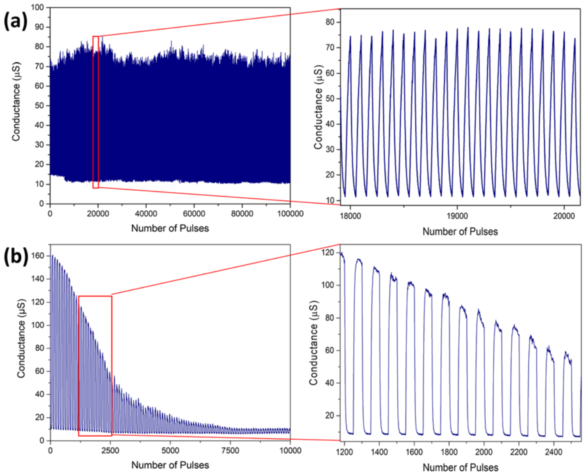

Fig. 2 Switching endurance of the polymer wire synaptic device (a) operated in EG (1000 cycles), (b) operated in water (100 cycles).

3.2 Reliability and performance metrics

Given the clear improvement in endurance under EG operation, we next evaluated the quantitative performance metrics of the device summarized in Fig. 3. The averaged cycle-to-cycle

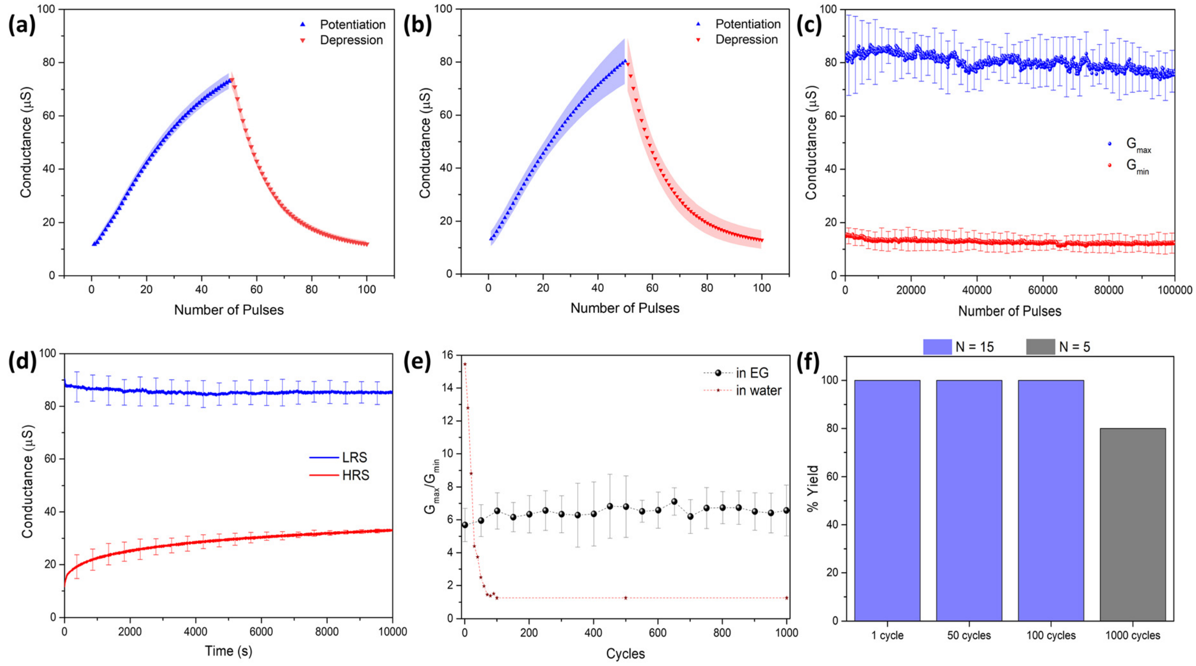

Fig. 3 Device reliability and statistical performance under EG operation. (a) Cycle-to-cycle variation across 1000 cycles, (b) device-to-device variation across 1000 cycles ($N = 3$), (c) distribution of G_{max} and G_{min}, (d) retention characteristics in the HRS and LRS state at 0.01 V_{read}, (e) evolution of G_{max}/G_{min} with cycling, (f) EG operated device % yield *vs.* cycle number with $G_{max}/G_{min} > 4$ as the functionality criterion, ($N = 15$ for over 100 cycles, $N = 5$ over 1000 cycles).

variation (Fig. 3a) is <5% across 1000 switching cycles. Whereas, the averaged device-to-device variation (Fig. 3b) was determined to be <15%. The observed device-to-device variation is likely associated with differences in polymer wire formation and electrode fabrication. In particular, variations in wire thickness and effective device geometry can influence the accessible switching window. The interfacial area affects the extent of doping and dedoping during operation. Hence, these factors likely contribute to the spread in conductance characteristics and should be more controlled in future work. As shown in Fig. 3c, the variation in G_{max} is larger than that in G_{min}. This suggests that the high-conductance state is more sensitive to structural and electrochemical inhomogeneity, whereas the low-conductance state is relatively more stable. One possible explanation is that the dedoping process proceeds more completely and reproducibly than the doping process, leading to a narrower distribution in G_{min} than in G_{max}.

The retention characteristics of the device were also evaluated at room temperature as shown in Fig. 3d. The low-resistance state (LRS) was maintained for up to 10^4 s whereas a slight drift was observed in the high-resistance state (HRS). This drift may originate from gradual relaxation of the ionic distribution after switching, which results in partial recovery of the conductance over time. To further assess operational stability, the evolution of G_{max}/G_{min} was examined and compared with that of the water-operated device (Fig. 3e). Although the water-operated device initially exhibited a larger G_{max}, its conductance ratio degraded rapidly and became inferior ($G_{max}/G_{min} < 4$) to that of the EG-operated device within 40 cycles. In contrast, the EG-operated device maintained a G_{max}/G_{min} of approximately between 4 and 8 over 1000 cycles. This suggests that EG has a more stable operation than the water-operated device under repeated cycling despite the smaller initial switching window. However, this should not be interpreted as evidence for the complete absence of degradation under extended operation beyond the tested cycle range. To provide an initial assessment of long-term environmental stability, a simple ambient storage measurement was also performed by comparing the switching behavior on day 1 and after 2 weeks of storage (Fig. S3). After 2 weeks, the initial switching characteristics were largely retained, although some reduction in G_{max} was observed at later cycles.

For the purpose of yield evaluation in this study, an operational criterion of $G_{max}/G_{min} > 4$ was adopted (Fig. 3f). Yields were evaluated over 100 switching cycles ($N = 15$), while longer endurance (>1000 cycles) was assessed using a smaller subset of devices ($N = 5$). Under these conditions, all devices remained operable over the initial 100-cycle range, whereas 80% of devices remained functional after 1000 cycles. In our measurements, water operation led to the degradation of G_{max}/G_{min} to < 2 within 100 cycles.

STP-related behavior was also examined to evaluate whether the device exhibits transient synaptic responses at short pulse intervals. However, increasing the interval between pulses did not result in noticeable conductance recovery. Hence, no clear STP behavior was observed. Instead, the conductance modulation was governed mainly by pulse-width-dependent LTD-like switching. This suggests that the conductance state is not strongly controlled by short-timescale relaxation processes in the present device. In addition, the capacitive response of the system further complicates the resolution of very short-timescale conductance measurements. These results indicate that the device is more suitable for stable conductance LTP modulation under repeated programming than for conventional STP operation.

Energy consumption is another important parameter since one of the key characteristics of the brain is its extremely low energy use.[43] The energy consumption per switching event is generally calculated by the following eqn (2);

$$E = \int VI(t)\mathrm{d}t \tag{2}$$

where V is the applied voltage, I is current flowing to the device and t is pulse width. Under the constant voltage pulse conditions in this work, the energy per switching event was estimated by expressing the current as $I = VG$. Therefore, the energy conusmption was estimated to be $E \approx V^2G_{\mathrm{ave}}t$, where G_{ave} is the averaged condutance during the switching. Using $V = 1.1$ V and $t = 25$ ms, the energy consumption of the device operated in EG is estimated to be ≈ 1.22 μJ per switching event.

The representative performance metrics for oxide-based and recent organic memristive devices are summarized in Table 1. The endurance of the present PEDOT–MeOH:SDBS polymer wire device (>1000 cycles) is lower than that of oxide-based memristors, which can reach 10^5–10^9 switching cycles. However, it is comparable to the moderate range in the reported studies for several organic and polymer-based memristive synaptic devices. Organic systems can also exhibit retention times on the order of 10^3–10^6 s and ON/OFF ratios ranging from approximately 10–10^6 depending on the material system and device architecture. Although the ON/OFF ratio of the present device is modest compared with some reported systems, it was sufficient for proof-of-concept CNN implementation (Section 3.5). The training process relied not only on state contrast but also on adequate weight resolution and repeatable conductance updates that allowed the device states to be used as analog kernel weights. In addition, the polymer-wire architecture offers high structural flexibility and potential relevance to three-dimensional wiring configurations, but switching endurance remains an important challenge for this class of wet-operating devices. The PEDOT–MeOH:SDBS device addresses this limitation to some extent by improving endurance under EG operation while preserving the configurational freedom of the polymer wire platform. Within this comparison, the present system is distinguished by its suspended polymer wire wet-operating configuration and by the explicit demonstration that the liquid medium strongly influences switching stability.

3.3 Morphological and structural characterization of the PEDOT–MeOH wire

To explain the high endurance and degradation phenomenon, the polymer wire was characterized before and after 100 switching cycles *via* electron microscopy and spectroscopy. The SEM image of the PEDOT–MeOH:SDBS polymer wire is shown in Fig. 4. The SEM of the pristine polymer wire was observed to have a slightly porous and rough surface (Fig. 4a and b). After 100 switching cycles in EG, the polymer surface developed aggregated granular domains with nodular protrusions (Fig. 4c and d). In contrast, cycling in water resulted in smoothened and deteriorated surface morphology (Fig. 4e and f). The granular morphology observed after cycling in EG is consistent with structural reorganization of the polymer/dopant system during operation. The maintained switching behavior indicates that conductive pathways were preserved. Such morphology is associated with maintained conductive domains and is favorable for repeated conductance modulation. By contrast, the smoother and more deteriorated morphology observed after cycling in water indicates progressive loss of the structural features associated with stable switching. This difference in morphology evolution strongly supports that the improved endurance in EG is linked to preservation of the switching-active polymer structure during repeated operation.

Furthermore, the conformational state of the polymer wire was probed using Raman spectroscopy as illustrated in Fig. 4g. The base PEDOT structure exists in two conformations. The benzoid form of PEDOT–MeOH has localized π bonds and a coiled structure and prevents effective polaron formation while the quinoid form is associated with greater backbone planarity and charge delocalization. Therefore, Raman peak shifts provide useful information on conformational changes relevant to conductance modulation. In the pristine state, vibrational modes above 1200 cm^{-1} are correlated to the polymer wire backbone. The peaks at 1380, 1439, and 1517 cm^{-1} are assigned to C_β–C_β, symmetric $C_\alpha = C_\beta$, and asymmetric $C_\alpha = C_\beta$ stretching modes, respectively.[21,44] These Raman features showed little or no significant shift, which suggests that the PEDOT–MeOH backbone remained comparatively well-preserved during EG operation. In contrast, operation in water exhibited a blue shift related to the backbone modes. Notably, C_β–C_β stretching shifted to 1400 cm^{-1}, symmetric $C_\alpha = C_\beta$ stretching to 1452 cm^{-1}, and

Table 1 Performance comparison against reported memristors and synaptic devices

Device class	Representative material	Endurance (cycles)	Retention	On/off ratio	Ref.
Oxide-based memristors	HfO_x, TaO_x, TiO_x	$\sim 10^5$–10^9	>10 years	10 to 10^3	35,36
Polymer/organic memristors	PEDOT: PSS, PMMA, PFN/PBS, PFcFE, PA-1	$\sim 10^3$–10^6	$\sim 10^3$–10^4 s	10^3 to 10^6	37,38
Organic memristor	PEDOT: PSS–ZnO NP hybrid film	>1000	10^4 s	NR	39
Organic memristor	ITO/AI4083:PH1000/Al	>500	10^4 s	~10	40
Organic memristor	ITO/TCNQ/Al	>1000	10^3 s	$\sim 10^3$	41
Organic memristor	Ag/Col–Gr NFs/FTO	>15 000	3×10^4 s	NR	42
Polymer wire wetware device	PEDOT–MeOH:SDBS wire in EG	>1000	10^4 s	~4–8	This work

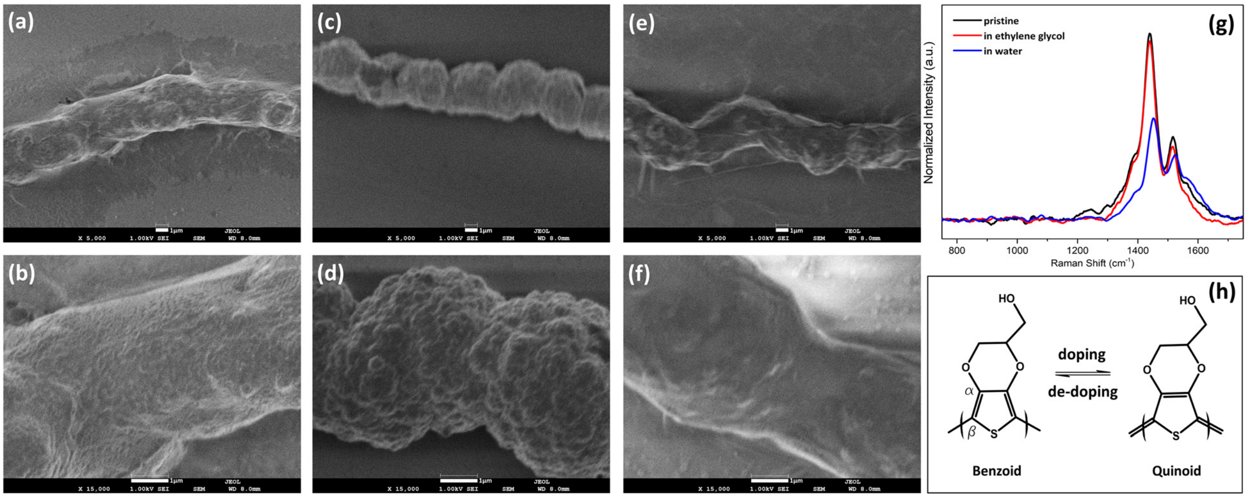

Fig. 4 Physical characterization of PEDOT–MeOH polymer wires before and after 100 switching cycles. SEM: (a) and (b) pristine wire at 5000× and 15 000× magnification; (c) and (d) after cycling in EG, at 5000× and 15 000× magnification; (e) and (f) after cycling in water, at 5000× and 15 000× magnification. (g) Raman spectra of pristine wires, operated in EG, and in water. (h) Schematic of the PEDOT–MeOH doping and dedoping process.

asymmetric $C_\alpha = C_\beta$ to 1525 cm^{-1}. These blue shifts are commonly associated with a reduced quinoid contribution and a shift toward a more benzoid-like backbone conformation[45] (Fig. 4h). Previous studies have also associated similar Raman shifts with morphology evolution and reduced structural order, which agrees with the SEM observations after aqueous cycling.[46] Together, the SEM and Raman results strongly support that operation in water accelerates structural deterioration during repeated switching, whereas operation in EG preserves the backbone and morphology more effectively. This structural preservation is aligned with the superior cycling endurance observed in EG.

3.4 Electrochemical characteristics of the PEDOT–MeOH wire

Two three-electrode setups were separately constructed to characterize the polymer wire in water and in EG. The polymer wire was grown only on one of the two Au electrodes, which also served as the working electrode. Restricting growth to a single working electrode provides a well-defined electrochemically active area and allowed us to probe the intrinsic response of a single polymer/electrolyte interface in a three-electrode configuration. Measuring a bridged wire in a three-electrode configuration would make *I–V*/EIS interpretation difficult since the response would contain contributions from two contacts and the bulk of the wire. Although the operational device is a two-terminal element where the polymer wire connects the two Au electrodes, the unconnected two-terminal pulsing and single-interface three-electrode measurements provide an approximation of the local interfacial processes that govern endurance in the connected device. We first performed electrochemical measurements on the initial state of the polymer wire. This was followed by rerouting to the two-terminal setup and then applying 100 cycles of potentiation–depression of 50 pulse trains per step. Finally, the setup was reverted to the three electrodes to evaluate the post-cycling changes in electrochemical behavior and impedance character. The *I–V* curves are shown in Fig. 5a for EG and Fig. 5c for water. The *I–V* measurements are included primarily to probe the underlying electrochemical redox characteristics of the PEDOT–MeOH:SDBS device before and after cycling. The synaptic functionality is represented through conductance state modulation *via* LTP/LTD behavior rather than the conventional excitatory/inhibitory current responses. Both systems show typical conducting polymer behavior with broad redox peaks and large capacitive currents.[47]

In EG, the *I–V* scan was measured at 100 mV s^{-1} from −1.5 to +1.0 V (*vs.* Ag/AgNO$_3$). Two distinct redox peaks appear at −0.4 V and −0.8 V are assigned to the dedoping and p-doping of PEDOT–MeOH:SDBS, respectively. After 100 switching cycles, these features persist with no detectable shift or loss, suggesting stable switching in EG. In water, measurement was performed on the potential sweep (100 mV s^{-1}) from −1.0 V to +1.0 V (*vs.* Ag/AgCl). Both anodic and cathodic doping peaks in the initial state occur at −0.2 V which indicates a highly reversible doping process. This CV profile is consistent with a prior report.[48] The peaks separated (oxidation process shifted to −0.24 V and reduction process to −0.4 V) after 100 switching cycles, which can be attributed to the progressive degradation of the polymer wire.[49] Additional minor peaks emerged at +0.44 V, −0.01 V and +0.17 V. These additional peaks likely reflect side reactions and degradation-related electrochemical processes in the polymer/dopant system. Repeated voltage stimulation may promote overoxidation of PEDOT–MeOH which has been associated with nucleophilic substitution at the thiophene ring and ring cleavage.[50]

To investigate the charge transfer and mass transport kinetics, EIS was measured at the midpoint of the redox couple (EG: −0.60 V DC bias; water: −0.20 V DC bias). The Nyquist plot for the polymer wire operated in EG and in water is shown in Fig. 5b and d, respectively. The equivalent circuit for both systems is described in Fig. 5e. Details of the fitting results

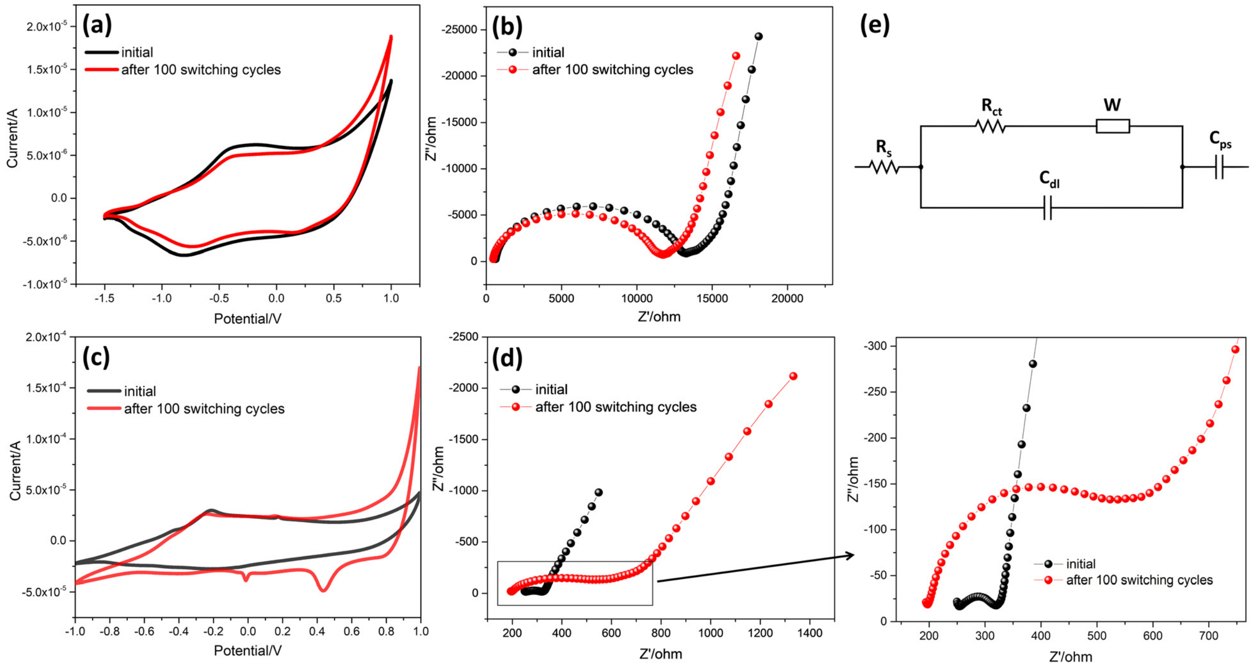

Fig. 5 *I–V* curve of the PEDOT–MeOH:SDBS wire in EG (*vs.* Ag/AgNO$_3$) in the initial state and after 100 switching cycles. (b) Nyquist plot of the corresponding impedance spectra measured at −0.6 V DC bias (1 × 10^5–1 × 10^{-1} Hz) and 150 mV amplitude. (c) *I–V* curve of the PEDOT–MeOH:SDBS wire in water (*vs.* Ag/AgCl) in the initial state and after 100 switching cycles. (d) Nyquist plot measured at −0.2 V DC bias (1 × 10^5–1 × 10^0 Hz) and 10 mV amplitude. (e) Equivalent circuit fitting for both the EG and water system.

and circuit element values are provided in Fig. S4 and Table S1. The high-frequency semicircle reflects the parallel circuit of charge transfer resistance (R_{ct}) and electric double layer capacitance (C_{dl}) at the PEDOT–MeOH:SDBS and electrolyte interface. This is followed by a low frequency tail modelled by Warburg impedance (W) defined as the diffusion limited process arising from the impedance between the bulk solution and polymer surface and electrode.[51] The uncompensated solution resistance is R_s. Electric double layer capacitance is represented by C_{dl} which is associated with non-faradaic currents from the adsorption of ions to the electrode surface and is connected in parallel with R_{ct} and W. A pseudocapacitive element (C_{ps}) is added to account for the fast capacitive nature indicated by the above 45° Warburg tail. In conducting polymers, the contribution of pseudocapacitance arises from rapid redox accompanied by anion insertion during oxidation and expulsion during reduction.[52,53]

The Nyquist plot in EG showed a much larger impedance than that in water, which is consistent with the higher viscosity and lower ionic mobility in EG. The usage of different solvent systems resulted in variability in the viscosity, ionic mobility, and dielectric constant. Hence, the quantitative discussion focuses on changes within each medium rather than direct comparison of absolute responses across media. In EG, the fitted R_{ct} decreased modestly from 12 240 to 10 730 Ω after 100 cycles. In water operation, R_{ct} increased markedly from 57.7 to 300.8 Ω and this is accompanied by an increase in the Warburg element from 1.746×10^{-4} to 3.851×10^{-4}. The lower initial R_{ct} in water is consistent with the larger initial switching window (G_{max}/G_{min}) since faster interfacial charge transfer can promote stronger early-cycle conductance modulation. However, the increase in R_{ct} and diffusion-related impedance after cycling indicate that this initially favorable electrochemical condition is not maintained during repeated operation. By contrast, the higher initial R_{ct} in EG is consistent with its smaller initial switching window. The comparatively modest change in R_{ct} after cycling aligns with the observed stable endurance behavior. Note that the post-cycling electrochemical measurements were performed after the final switching step ended in the low-resistance state, which should be considered when interpreting the measured response. Overall, these results indicate comparatively limited electrochemical change in EG and substantially greater diffusion-limited and charge-transfer deterioration in water after cycling. Together with the *I–V* peak separation and emergence of secondary peaks, the electrochemical results support more severe degradation under aqueous operation than under EG. This EIS analysis provides electrochemical support for the observed endurance difference and is interpreted together with the structural and spectroscopic results.

3.5 CNN implementation using the synaptic polymer wire

We evaluated the feasibility of the high endurance device by using the conductance states of the polymer wires for a machine learning architecture. CNNs are a widely adopted class of machine learning architecture for image classification, speech recognition and language processing.[54] Their accuracy arises from learning spatial patterns through successive convolutional layers that extract hierarchical features. A convolution applies a kernel (a small weight matrix) that slides across the input and computes dot products to produce feature maps. After convolution, the extracted features are typically passed to fully connected layers for classification. Kernels are particularly suitable for physical weight implementation since they use local connectivity and weight sharing. This results in fewer trainable parameters than using the fully connected layers, which reduces the number of weights and training time. Most studies rely on simulation to evaluate device feasibility in machine learning tasks.[55] However, here we integrated the conductance states bottom up as CNN kernels and validated within the CNN workflow. In this context, the present device is proposed as a candidate for analog weight storage and update in CNN kernels rather than as a direct demonstration of complete CNN operation.

The CNN architecture was implemented using a hardware-in-the-loop CNN architecture illustrated in Fig. 6a. Sixteen polymer-wire synapses provided the 3 × 3 kernel weights during training. Due to device constraints associated with device fabrication, the kernels were selectively masked with some weights to be inactive (see Fig. S7). This streamlines the device and introduces sparsity to efficiently capture feature representation and reduce the implementation of physical weights. The dataset comprised 5 × 5-digit images with five samples per class (Fig. S6). This toy dataset was intentionally designed for device-in-the-loop applications instead of large-scale benchmarking tasks. Its small size makes the required write cycles manageable while preserving the essential features of hardware-in-loop training. After each convolution step, feature maps were pooled and passed to a fully connected layer for the classification. The weights were updated using stochastic gradient descent with backpropagation. Because the individual wires exhibited non-linear conductance updates, each weight update used a program-and-verify loop that iteratively pulsed to change the conductance until it falls within ±1% of the target. The resulting updated weights were carried for the next cycle of epoch.

Training behavior is summarized in Fig. 6b and c. The accuracy rose rapidly in the early epochs and plateaued after 60 epochs. This suggests the limitation of the 5 × 5 input size, which cannot encode key digit cues such as unique curvature, junctions, and endpoints. Therefore, gradients beyond this point carry limited class-separating information. At the final epoch (450), the training reached 96% accuracy indicating effective class separation under these constraints. Cross entropy loss also decreased smoothly during the training. A falling loss alongside stabilizing accuracy indicates that predictions became more confident and better separated. We also performed a simulated workflow by updating the weights using software once per epoch with randomized ±1% noise to mimic program-and-verify. The simulated accuracy and loss confirm the hardware results. Note that the curves were smoother in the simulation while the actual hardware exhibited small fluctuations due to the noise and device variability. The confusion matrix (Fig. 6d) at the final epoch summarizes the classification performance by comparing predicted and true digit labels for each class. Due to the low spatial resolution of the 5 × 5 inputs, the digit "1" was misclassified as "2" and digit "3" as "5" since their pooled feature maps become difficult to distinguish. All other digits

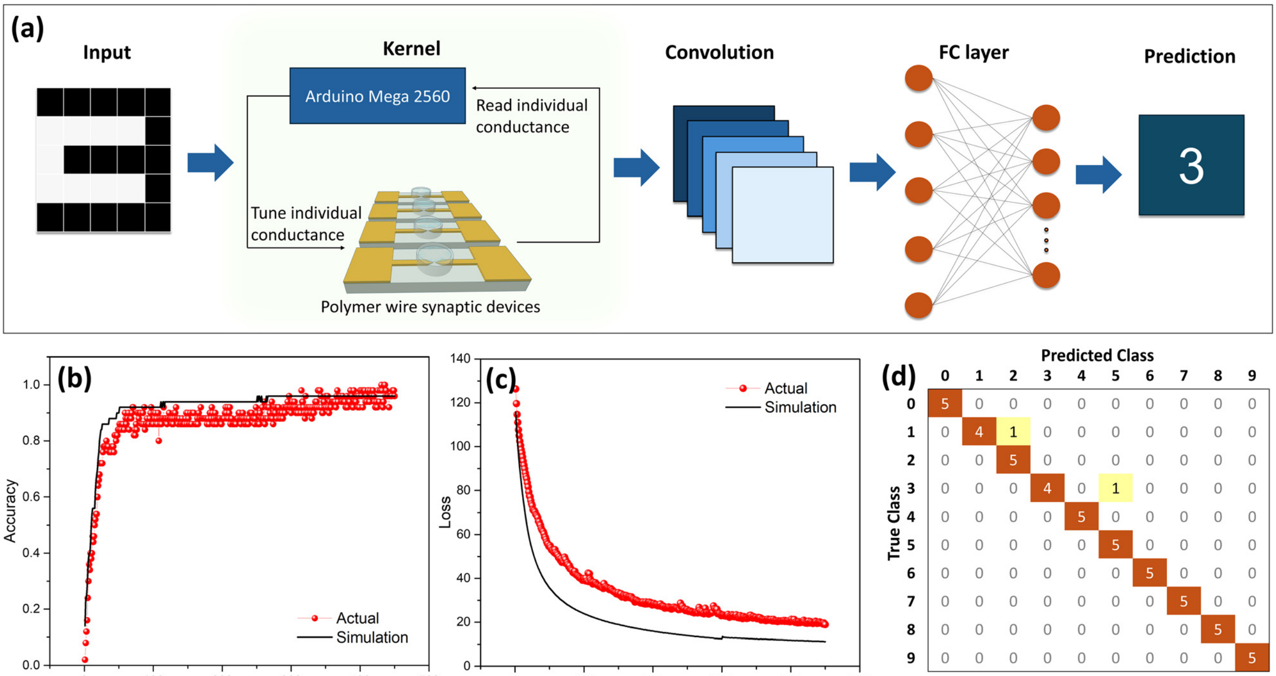

	0	1	2	3	4	5	6	7	8	9
0	5	0	0	0	0	0	0	0	0	0
1	0	4	1	0	0	0	0	0	0	0
2	0	0	5	0	0	0	0	0	0	0
3	0	0	0	4	0	1	0	0	0	0
4	0	0	0	0	5	0	0	0	0	0
5	0	0	0	0	0	5	0	0	0	0
6	0	0	0	0	0	0	5	0	0	0
7	0	0	0	0	0	0	0	5	0	0
8	0	0	0	0	0	0	0	0	5	0
9	0	0	0	0	0	0	0	0	0	5

Fig. 6 (a) Custom CNN architecture using the polymer wire synaptic device, (b) accuracy of the training after 450 epochs, (c) loss function of the training after 450 epochs, and (d) confusion matrix results at the final epoch using the actual device.

were correctly classified. Higher input resolution and kernels additions are expected to improve accuracy at the cost of longer runtime and additional write cycles. The successful mapping of the polymer wire conductance states directly to the CNN kernels preserves true device physics during learning and yields results that extend beyond pure simulation. In addition, the physical CNN implementation demonstrated here provides a practical option that future studies may adopt when exploring wetware-based neuromorphic devices and architectures.

4. Conclusions

We successfully fabricated a PEDOT–MeOH:SDBS wetware device capable of exhibiting long-term potentiation and depression (LTP/D) *via* conductance switching. Switching arises from making the polymer wire asymmetric, which causes uneven doping efficiency and introduces a directional write response. Operation in EG enables moderate switching endurance (≥1000 cycles). This improved endurance was consistent with the preserved impedance response, stable *I–V* curves, and structural evolution observed after cycling. In contrast, operation in water led to rapid degradation of the conductance switching behavior. Structural and electrochemical characterization showed that aqueous operation was associated with a smoother and more deteriorated morphology, Raman shifts toward a less delocalized backbone state, the emergence of additional electrochemical features, and increased charge-transfer resistance after cycling. The conductance states of the polymer wire device (operated in EG) were physically mapped to kernel weights in a custom CNN for digit recognition. The network achieved 96% classification accuracy over 450 epochs, demonstrating the feasibility of using the polymer-wire device as a non-volatile analog weight element in a hardware-in-the-loop implementation. To summarize, these results show that the liquid operating medium plays a decisive role in the repeated switching stability of polymer-wire wetware synapses. Specifically, EG supported a more stable conductance modulation than water under the tested conditions. Future work should further examine the roles of solvent properties, device geometry, and larger device arrays, as well as extend the hardware-in-the-loop framework to more complex image datasets such as MNIST.

Author contributions

Adrian D. Go: methodology, investigation, data curation, formal analysis, writing – original draft. Seiya Watanabe: writing – review and editing, formal analysis, project administration, funding acquisition. Hiroyuki S. Kato: writing – review and editing, resources, formal analysis. Megumi Akai-Kasaya: conceptualization, supervision, methodology, writing – review and editing, project administration, funding acquisition.

Conflicts of interest

There are no conflicts to declare.

Data availability

The authors declare that the supporting data have been provided as part of the supplementary information (SI). Supplementary information is available. See DOI: https://doi.org/10.1039/d5ma01448d.

Acknowledgements

This work was supported by JSPS KAKENHI Grant Numbers JP 24K03009 and JP25K15261. A part of this work was conducted in Advanced Research Infrastructure for Materials and Nanotechnology Open Facilities in The University of Osaka, supported by the ARIM Program of the Ministry of Education, Culture, Sports, Science and Technology (MEXT), Japan, Grant Number JPMXP1225OS1009. This work was supported by JST CREST JPMJCR21B5, Japan. We would like to acknowledge Professor Masateru Taniguchi and Dr Sanae Murayama (Taniguchi Laboratory, The University of Osaka) for their assistance in the LED lithography patterning of the substrate. The SEM analyses were performed at the Analytical Instrument Facility, Graduate School of Science, The University of Osaka. A. G. acknowledges support from the Japanese Government (MEXT) Scholarship Program.

Notes and references

1 Y. LeCun, Y. Bengio and G. Hinton, *Nature*, 2015, **521**, 436–444.
2 A. Bin Rashid and M. A. K. Kausik, *Hybrid Adv.*, 2024, **7**, 100277.
3 A. de Vries, Cell Press, 2023, preprint, DOI: 10.1016/j.joule.2023.09.004.
4 A. Sebastian, M. Le Gallo, R. Khaddam-Aljameh and E. Eleftheriou, *Nat. Nanotechnol.*, 2020, **15**, 529–544.
5 J. Ajayan, D. Nirmal, B. K. Binola and S. Sreejith, *Microelectronics J.*, 2022, **130**, 105634.
6 Z. Kuncic and T. Nakayama, *Taylor and Francis Ltd*, 2021, preprint, DOI: 10.1080/23746149.2021.1894234.
7 Q. Wan, M. T. Sharbati, J. R. Erickson, Y. Du and F. Xiong, *Wiley-Blackwell*, 2019, preprint, DOI: 10.1002/admt.201900037.
8 S. Ali, M. A. Ullah, A. Raza, M. W. Iqbal, M. F. Khan, M. Rasheed, M. Ismail and S. Kim, *Multidisciplinary Digital Publishing Institute (MDPI)*, 2023, preprint, DOI: 10.3390/nano13172443.
9 L. Wang, S.-R. Lu and J. Wen, *Nanoscale Res. Lett.*, 2017, **12**, 347.
10 M. Lederer, T. Kampfe, T. Ali, F. Muller, R. Olivo, R. Hoffmann, N. Laleni and K. Seidel, *IEEE Trans. Electron Devices*, 2021, **68**, 2295–2300.
11 H. Ha, J. Pyo, Y. Lee and S. Kim, *Materials*, 2022, **15**(24), 9087.
12 L. Gao, M. Wu, X. Yu and J. Yu, *Int. J. Extreme Manuf.*, 2024, **6**, 012005.

13 S. Yu and E. L. Ratcliff, *ACS Appl. Mater. Interfaces*, 2021, **13**, 50176–50186.

14 L. Cao, X. Q. Wang, Z. X. Wu, B. Y. Lu, L. Shen, F. Z. Cai, J. K. Xu, J. L. Wang and G. Zhang, *React. Funct. Polym.*, 2024, **195**, 105813.

15 J. Cameron and P. J. Skabara, *Mater. Horiz.*, 2020, **7**, 1759–1772.

16 A. Schaarschmidt, A. A. Farah, A. Aby and A. S. Helmy, *J. Phys. Chem. B*, 2009, **113**, 9352–9355.

17 E. Zheng, P. Jain, H. Dong, Z. Niu, S. Chen, S. Zhong and Q. Yu, *ACS Appl. Polym. Mater.*, 2019, **1**, 3103–3114.

18 E. Tomsik, P. Pospíšil, E. Tomšík, S. Nešpůrek and L. Kubáč, Chemical oxidation of EDOT-MeOH monomer. Influence of the polymerization process on the electrical properties of PEDOT-MeOH, 2013.

19 H. Dong, E. Zheng, Z. Niu, X. Zhang, Y. Y. Lin, P. Jain and Q. Yu, *ACS Appl. Mater. Interfaces*, 2020, **12**, 17571–17582.

20 Y.-Y. Yao, L. Zhang, Z.-F. Wang, J.-K. Xu and Y.-P. Wen, *Chin. Chem. Lett.*, 2014, **25**, 505–510.

21 S. Yu, Y. Chen, Y. Yang, Y. Yao and H. Song, *RSC Adv.*, 2022, **12**, 15517–15525.

22 Y. J. Lee, Y. H. Kim and E. K. Lee, *Macromol. Rapid Commun.*, 2024, **45**(17), 2400165.

23 H. F. de, P. Barbosa, M. El Abdouni, A. Schander and B. Lüssem, *Adv. Electron. Mater.*, 2026, **12**(1), e00507.

24 X. Luo, J. Ming, J. Gao, J. Zhuang, J. Fu, Z. Ren, H. Ling and L. Xie, *Front. Neurosci.*, 2022, **16**, 1016026.

25 Z. Wang and F. Yan, *Small Methods*, 2026, **10**(7), e01966.

26 S. L. Bidinger, S. Han, G. G. Malliaras and T. Hasan, *Appl. Phys. Lett.*, 2022, **120**(7), 073302.

27 F. Mariani, F. Decataldo, F. Bonafè, M. Tessarolo, T. Cramer, I. Gualandi, B. Fraboni and E. Scavetta, *American Chemical Society*, 2023, preprint, DOI: 10.1021/acsami.3c10576.

28 S. Watanabe, H. Shibakita, N. Hagiwara, R. Nakajima, H. S. Kato and M. Akai-Kasaya, *ACS Appl. Mater. Interfaces*, 2024, **16**(40), 54636–54644.

29 K. Janzakova, I. Balafrej, A. Kumar, N. Garg, C. Scholaert, J. Rouat, D. Drouin, Y. Coffinier, S. Pecqueur and F. Alibart, *Nat. Commun.*, 2023, **14**(1), 8143.

30 N. Hagiwara, T. Asai, K. Ando and M. Akai-Kasaya, *Adv. Funct. Mater.*, 2023, **33**(42), 2300903.

31 S. van Reenen, M. Scheepers, K. van de Ruit, D. Bollen and M. Kemerink, *Org. Electron.*, 2014, **15**, 3710–3714.

32 N. A. N. Asri, B. Amir, A. S. Ramli, M. F. Safian, A. Zakaria, N. A. Jani and M. M. Mahat, *J. Phys.: Conf. Ser.*, 2022, **2169**, 012036.

33 N. Hagiwara, S. Sekizaki, Y. Kuwahara, T. Asai and M. Akai-kasaya, *Polymers*, 2021, **13**, 1–10.

34 S. L. Jackman and W. G. Regehr, *Neuron*, 2017, **94**, 447–464.

35 Z. Wang, Z. Li, Z. Xia, X. Sun, J. Meng and T. Wang, *Chip*, 2025, 100183.

36 R. Islam, H. Li, P.-Y. Chen, W. Wan, H.-Y. Chen, B. Gao, H. Wu, S. Yu, K. Saraswat and H.-S. Philip Wong, *J. Phys. D: Appl. Phys.*, 2019, **52**, 113001.

37 K. Gou, Y. Li, H. Song, R. Lu and J. Jiang, *iScience*, 2024, **27**, 111327.

38 Y. Chen, G. Liu, C. Wang, W. Zhang, R.-W. Li and L. Wang, *Mater. Horiz.*, 2014, **1**, 489.

39 J. Fan, J. Feng, Y. Gao, Z. Zhang, S. Xue, G. Cai and J. S. Zhao, *ACS Appl. Nano Mater.*, 2024, **7**, 5661–5668.

40 M. K. Rahmani, S. A. Khan, H. Kim, M. U. Khan, J. Kim, J. Bae and M. H. Kang, *Org. Electron.*, 2023, **114**, 106730.

41 N. Pandit, R. Mandal, A. Pal, A. Mandal, R. Nath and B. Mukherjee, *Org. Electron.*, 2026, **149**, 107364.

42 S. M. Mane, A. A. Bagade, K. A. Rokade, S. S. Mahajan, P. D. Halagale, S. A. Surve, P. P. Sonawane, K. A. Nirmal, A. A. Jeffery, Y.-H. Ahn, T. G. Kim and T. D. Dongale, *Mater. Today Nano*, 2026, **33**, 100746.

43 B. Tang, X. Li, J. Liao and Q. Chen, *ACS Appl. Electron. Mater.*, 2022, **4**, 598–605.

44 Y. Zhang, H. Zhang, F. Jiang, W. Zhou, R. Wang, J. Xu, X. Duan, Y. Wu and Y. Ding, *Ionics*, 2020, **26**, 3631–3642.

45 Y. Shi, Y. Zhou, Z. Che, J. Shang, Q. Wang, F. Liu and Y. Zhou, *Mater. Lett.*, 2022, **308**, 131106.

46 M. Kong, M. Garriga, J. S. Reparaz and M. I. Alonso, *ACS Omega*, 2022, **7**, 39429–39436.

47 G. Li and P. G. Pickup, *Phys. Chem. Chem. Phys.*, 2000, **2**, 1255–1260.

48 Y. Xiao, X. Cui, J. M. Hancock, M. Bouguettaya, J. R. Reynolds and D. C. Martin, *Sens. Actuators, B*, 2004, **99**, 437–443.

49 S. Garreau, G. Louarn, J. P. Buisson, G. Froyer and S. Lefrant, *Macromolecules*, 1999, **32**, 6807–6812.

50 R. Holze, *Polymers*, 2022, **14**, 1584.

51 N. O. Laschuk, E. B. Easton and O. V. Zenkina, *RSC Adv.*, 2021, **11**, 27925–27936.

52 T.-H. Le, Y. Kim and H. Yoon, *Polymers*, 2017, **9**(4), 150.

53 X. Fan, P. Ohlckers and X. Chen, *Appl. Sci.*, 2020, **10**, 1208.

54 M. Krichen, *Computers*, 2023, **12**, 151.

55 M. K. Rahmani, S. A. Khan, H. Kim, M. U. Khan, J. Kim, J. Bae and M. H. Kang, *Org. Electron.*, 2023, **114**, 106730.